Structure of low-lying states in ^{140}Sm studied by Coulomb excitation

M. Klintefjord,[1] K. Hadyńska-Klęk,[1,2] A. Görgen,[1,*] C. Bauer,[3] F. L. Bello Garrote,[1] S. Bönig,[3] B. Bounthong,[4,5] A. Damyanova,[6] J.-P. Delaroche,[7] V. Fedosseev,[8] D. A. Fink,[8] F. Giacoppo,[1,†] M. Girod,[7] P. Hoff,[9] N. Imai,[10] W. Korten,[11] A.-C. Larsen,[1] J. Libert,[7] R. Lutter,[12] B. A. Marsh,[8] P. L. Molkanov,[13] H. Naïdja,[4,5] P. Napiorkowski,[14] F. Nowacki,[4,5] J. Pakarinen,[15,16] E. Rapisarda,[8,17] P. Reiter,[18] T. Renstrøm,[1] S. Rothe,[8,19] M. D. Seliverstov,[13] B. Siebeck,[18] S. Siem,[1] J. Srebrny,[14] T. Stora,[8] P. Thöle,[18] T. G. Tornyi,[1] G. M. Tveten,[1] P. Van Duppen,[17] M. J. Vermeulen,[20] D. Voulot,[8] N. Warr,[18] F. Wenander,[8] H. De Witte,[17] and M. Zielińska[11]

[1]*Department of Physics, University of Oslo, N-0316 Oslo, Norway*
[2]*INFN, Laboratori Nazionali di Legnaro, I-35020 Legnaro, Italy*
[3]*Institut für Kernphysik, Technische Universität Darmstadt, Darmstadt D-64289, Germany*
[4]*IPHC, Université de Strasbourg, IPHC, 23 Rue du Loess F-67037 Strasbourg, France*
[5]*IPHC, CNRS, UMR7178, F-67037 Strasbourg, France*
[6]*University of Geneva, Bd du Pont-d'Arve 40, CH-1211 Genéve, Switzerland*
[7]*CEA, DAM, DIF, F-91297 Arpajon, France*
[8]*CERN, CH-1211 Geneva 23, Switzerland*
[9]*Department of Chemistry, University of Oslo, N-0316 Oslo, Norway*
[10]*High Energy Accelerator Research Organization (KEK), Oho 1-1, Tsukuba, Ibaraki 305-0801, Japan*
[11]*CEA Saclay, IRFU, SPHN, F-91191 Gif-sur-Yvette, France*
[12]*Fakultät für Physik, Ludwig-Maximilians-Universität München, D-85740 Garching, Germany*
[13]*Petersburg Nuclear Physics Institute, NRC Kurchatov Institute, Gatchina 188300, Russia*
[14]*Heavy Ion Laboratory, University of Warsaw, 02-093 Warsaw, Poland*
[15]*University of Jyväskylä, Department of Physics, P.O. Box 35, FIN-40014 University of Jyväskylä, Finland*
[16]*Helsinki Institute of Physics, University of Helsinki, P.O. Box 64, FIN-00014 Helsinki, Finland*
[17]*Instituut voor Kern- en Stralingsfysica, KU Leuven, Leuven B-3001, Belgium*
[18]*Institut für Kernphysik, Universität zu Köln, Köln D-50937, Germany*
[19]*Institut für Physik, Johannes Gutenberg-Universität Mainz, D-55128 Mainz, Germany*
[20]*Department of Physics, University of York, York YO10 5DD, United Kingdom*

The electromagnetic structure of ^{140}Sm was studied in a low-energy Coulomb excitation experiment with a radioactive ion beam from the REX-ISOLDE facility at CERN. The 2^+ and 4^+ states of the ground-state band and a second 2^+ state were populated by multistep excitation. The analysis of the differential Coulomb excitation cross sections yielded reduced transition probabilities between all observed states and the spectroscopic quadrupole moment for the 2_1^+ state. The experimental results are compared to large-scale shell model calculations and beyond-mean-field calculations based on the Gogny D1S interaction with a five-dimensional collective Hamiltonian formalism. Simpler geometric and algebraic models are also employed to interpret the experimental data. The results indicate that ^{140}Sm shows considerable γ softness, but in contrast to earlier speculation no signs of shape coexistence at low excitation energy. This work sheds more light on the onset of deformation and collectivity in this mass region.

I. INTRODUCTION

The shape of atomic nuclei is a fundamental property which is governed by the interplay between single-particle and collective degrees of freedom. Nuclei with closed proton and neutron shells are spherical in their ground state, whereas the occupation of shape-driving orbitals causes nuclei with open shells to be deformed. The majority of deformed nuclei is found to have prolate (elongated) quadrupole shapes. For heavy nuclei with $Z, N > 50$, oblate ground-state shapes are rare and mostly found in regions with holes in high-spin, low-Ω orbitals near the top of the proton and neutron shells [1]. Mean-field calculations based on Gogny [2] or Skyrme [3] interactions predict oblate ground states, e.g., for platinum and mercury isotopes with $N > 106$ and for $N \approx 78$ and $N \approx 120$ isotones with $Z > 60$.

In certain regions of the nuclear chart, prolate and oblate shapes are found to coexist at low excitation energy. Shape coexistence at low energy can generally be expected when there is a competition between an energy gap and a residual

---

*andreas.gorgen@fys.uio.no

†Present address: Helmholtz Institute, D-55099 Mainz, and GSI, D-64291 Darmstadt, Germany.

interaction that favors excitations across the gap [4,5]. Prominent examples for shape coexistence based on this mechanism are found in the $Z = 82$ region near neutron midshell, e.g., in ^{186}Pb [6] and the neighboring mercury isotopes [7]. Not surprisingly these nuclei lie in the region where mean-field calculations predict the transition from prolate to oblate ground-state shapes. From these observations one may expect to find shape coexistence also in the $N \approx 78$ region near proton midshell, where the role of protons and neutrons is interchanged. However, clear experimental indication for shape coexistence near the ground state is lacking in this region, and it was argued that the $Z = 64$ subshell closure could explain the absence of shape coexistence in this region [4]. There is, however, evidence for shape coexistence at higher excitation energy in the $N = 78$ isotones ^{140}Sm and ^{142}Gd. Two isomeric 10^+ states based on the configuration $(\pi h_{11/2})^2$ and $(\nu h_{11/2})^{-2}$ are found in both nuclei [8]. Lifetime measurements found the rotational bands built on top of the 10^+ states with proton-particle and neutron-hole character in ^{140}Sm to be consistent with prolate and oblate shape, respectively [9]. The shape associated with the states in the ground-state band of ^{140}Sm below the 10^+ isomers is not clear and is the subject of the present investigation.

Relativistic mean-field calculations restricted to axial deformations predicted the ground state of ^{140}Sm to have oblate shape, whereas prolate deformation was found to develop rapidly in the lighter samarium isotopes with $N \leqslant 76$ [10]. More recent relativistic Hartree-Fock-Bogoliubov (HFB) calculations find a smooth transition from spherical ^{144}Sm to well-deformed prolate ^{134}Sm with a γ-soft potential energy surface for the transitional nucleus ^{140}Sm [11]. The observation and tentative assignment of a (2_2^+) state at 990 keV and a (3_1^+) state at 1599 keV in ^{140}Sm following the β decay of ^{140}Eu was interpreted as evidence for a low-lying γ band [12]. The observation was supported by triaxial-rotor calculations based on a Woods-Saxon potential, which reproduced the excitation energies of the presumed γ band and also found the potential energy surface for ^{140}Sm to be soft in the triaxial degree of deformation [12]. However, a subsequent β-decay experiment revised the earlier spin values and tentatively assigned spin-parity (0^+) and (2^+) to the states at 990 and 1599 keV, respectively [13]. The presence of a second 0^+ state at such low excitation energy is somewhat surprising when comparing with the systematics of excited states in neighboring nuclei. On the other hand, such a low-lying 0_2^+ state could indicate the presence of shape coexistence near the ground state of ^{140}Sm. The spin assignments for the two states in question were clarified in a recent measurement of γ-γ angular correlations following the β decay of ^{140}Eu, which firmly showed that the state at 990 keV in ^{140}Sm has spin-parity 2^+ and the state at 1599 keV $0^{(+)}$ [14]. The level scheme for the states of the ground-state band and the lowest non-yrast states is shown in Fig. 1.

The collectivity of the 2_1^+ state in ^{140}Sm was studied in a recent recoil distance lifetime measurement [15]. The resulting $B(E2; 2_1^+ \to 0_1^+)$ value and its comparison to the neighboring samarium isotopes indicates a gradual onset of deformation when removing neutrons from the closed-shell nucleus ^{144}Sm$_{82}$. The experimental $B(E2; 2_1^+ \to 0_1^+)$
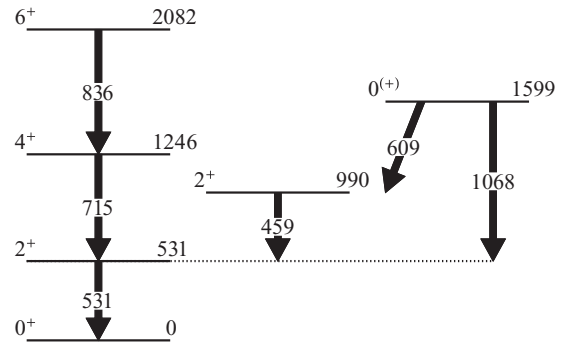

FIG. 1. Partial level scheme showing low-lying states in ^{140}Sm. The spin assignments for the excited states at 990 and 1599 keV are taken from a recent angular correlation measurement [14].

values for the entire chain of neutron-deficient samarium isotopes are well reproduced by microscopic HFB calculations with the Gogny D1S interaction with mapping to the five-dimensional collective Hamiltonian (5DCH) for quadrupole excitations [15]. The theoretical calculations explain the onset of quadrupole collectivity in the samarium isotopes below $N = 82$ by a gradual shape transition from large prolate deformation with axial symmetry for the lightest isotopes to spherical shape in ^{144}Sm, with the triaxial degree of freedom becoming more important as $N = 82$ is approached. The Gogny 5DCH calculations find average quadrupole parameters of $\langle \beta \rangle = 0.17$ and $\langle \gamma \rangle = 29°$ for the ground state of ^{140}Sm [15].

It appears that the onset of deformation in the samarium isotopes is different above and below the neutron shell closure. For $N > 82$ the samarium nuclei show an abrupt increase in deformation at $N = 90$, whereas the onset of deformation is more gradual for $N < 82$ with apparent triaxiality in the transitional region around ^{140}Sm. The rapid increase in deformation from $N = 88$ to $N = 90$ in the samarium and gadolinium isotopes can be explained by the occupation of proton and neutron spin-orbit partner orbitals which causes the disappearance of the $Z = 64$ subshell closure for $N \geqslant 90$ [16]. The transitional nucleus ^{152}Sm was identified as one of the best realizations of the so-called X(5) critical point symmetry [17,18], which represents a first-order phase transition from a spherical vibrational to a deformed rotational nucleus. The analysis of excitation spectra for the samarium isotopes with $N < 82$ using the interacting boson approximation (IBA) found model parameters for ^{138}Sm and ^{140}Sm that place these nuclei between the U(5) and the SO(6) limits of the IBA [19], i.e., at the transition between a spherical vibrator and a γ-soft vibrator characterized by the so-called E(5) critical point symmetry [20]. However, without any experimental $B(E2)$ values beyond the 2_1^+ state and uncertain spin assignments for the lowest non-yrast states it was not possible to evaluate a possible E(5) character for ^{140}Sm.

In this article we present the results of a Coulomb excitation experiment using a radioactive ^{140}Sm beam, which provides several $B(E2)$ values and also the spectroscopic quadrupole moment for the 2_1^+ state. Low-energy Coulomb excitation is an ideal method to study the collectivity and deformation in this nucleus, because both yrast and non-yrast states can

be populated and transition probabilities extracted without interference from the isomeric 10^+ states. The comparison of the experimental results with theoretical calculations sheds more light on the onset of deformation and collectivity in this mass region. The article is organized as follows: The experimental details and data analysis are described in Sec. II. The extraction of electromagnetic matrix elements from the Coulomb excitation yields is described in Sec. III. The results are discussed and compared to theoretical calculations in Sec. IV, followed by a summary and conclusions in Sec. V.

II. EXPERIMENTAL DETAILS

The application of the isotope separation on-line (ISOL) technique in combination with selective laser ionization and post-acceleration made it possible to study the electromagnetic properties of ^{140}Sm by Coulomb excitation. Radioactive ^{140}Sm atoms with a half-life of 14.8 min were produced at the CERN-ISOLDE facility by spallation of a primary tantalum target with 1.4-GeV protons from the PS Booster. Samarium atoms were selectively ionized using the Resonance Ionization Laser Ion Source (RILIS) [21], which was equipped with a GdB$_6$ low-work function cavity [22] to reduce the surface ionization of isobaric impurities. After selection of mass $A = 140$ using the general purpose separator GPS, the ions were bunched, cooled, and trapped in the REXTRAP [23], and then further ionized to charge state 34^+ using the EBIS charge breeder [24]. Finally the highly charged ^{140}Sm ions were accelerated to an energy of $2.85A$ MeV in the REX linear accelerator [25]. An average intensity of 2×10^5 particles per second was achieved over a beam time of approximately 100 h.

The ^{140}Sm projectiles were scattered on a secondary ^{94}Mo target of $2\,\text{mg/cm}^2$ thickness. Both ^{140}Sm projectiles and ^{94}Mo target nuclei were excited in the low-energy Coulomb excitation reaction. The distance of closest approach of 19.2 fm between the projectiles and target nuclei for the given reaction parameters is larger than the distance of 17.2 fm, which is obtained by applying the safe distance separation criterion [26],

$$d > 1.25\big(A_p^{1/3} + A_t^{1/3}\big) + 5 \text{ fm}, \qquad (1)$$

where A_p and A_t are the mass numbers of the projectile and target, respectively. Under these conditions, it is safe to neglect all influence of the strong nuclear force and assume that the excitation process can be described by a pure electromagnetic interaction.

Gamma rays from excited states in the ^{140}Sm projectiles and ^{94}Mo target nuclei were detected in the MINIBALL HPGe detector array [27], which at the time of the experiment consisted of seven triple-cluster modules, each of which comprised three sixfold segmented germanium crystals. An energy and efficiency calibration for the germanium detectors was performed using standard ^{152}Eu and ^{133}Ba sources. An annular double-sided silicon strip detector (DSSSD) of 1000-μm thickness was mounted in the MINIBALL target chamber and used to detect both scattered projectiles and recoiling target nuclei. The DSSSD consisted of four individual quadrants with each 16 concentric annular strips on the front side and 12 azimuthal sector strips on the back side. The annular strips
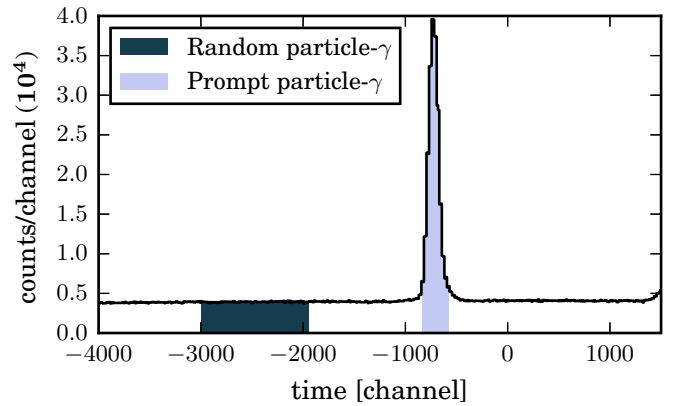

FIG. 2. Particle-γ coincidence time spectrum. A normalized fraction of the random gate was used for background subtraction.

had a strip pitch of 2 mm and the azimuthal strips covered $3.5°$ each. In total, the DSSSD covered $5000\,\text{mm}^2$ with an active area of 93% [28]. The detector was mounted in forward direction at a distance of 25.2 mm from the target, covering the angular range from $19.7°$ to $58.4°$ in the laboratory frame. In the center-of-mass frame, the angular coverage corresponded to $49.7° < \theta_{\text{c.m.}} < 146°$ for the detection of ^{140}Sm projectiles and $63.1° < \theta_{\text{c.m.}} < 140.7°$ for the detection of recoiling target nuclei.

The data acquisition was triggered and events were built when the MINIBALL and DSSSD detectors gave coincident signals. Prompt particle-γ coincidences were selected by applying a prompt gate in the time spectrum, and background from random coincidences was subtracted as shown in Fig. 2. The energy spectrum for particles as a function of scattering angle measured with one DSSSD quadrant in coincidence with γ rays detected in MINIBALL is shown in Fig. 3. The contours illustrate the separation and selection for scattered projectiles and recoiling target nuclei. The innermost annular strips of the DSSSD could not be used in the further analysis because
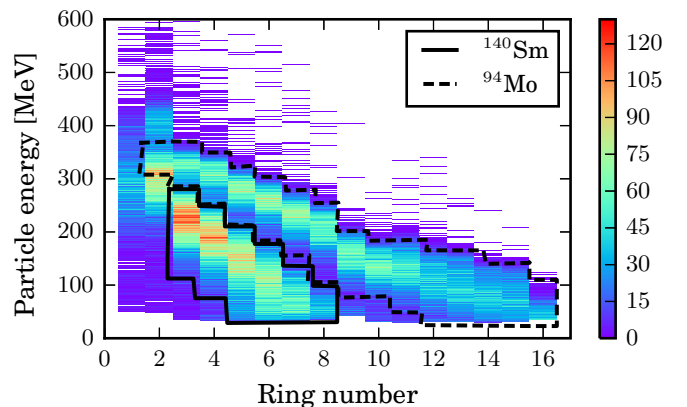

FIG. 3. Energy spectra of particles detected in the DSSSD as a function of the laboratory scattering angle. The cuts to select between detected ^{140}Sm projectiles and recoiling ^{94}Mo target nuclei are marked. Ring number 1 corresponds to laboratory angle $19.7°$ and ring 16 to laboratory angle $58.4°$.
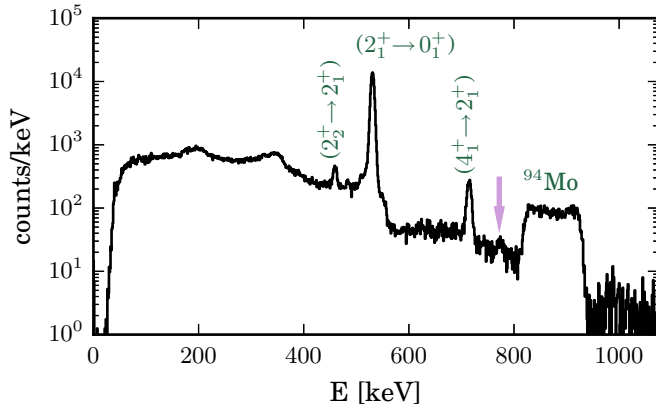
FIG. 4. Background subtracted γ-ray spectrum in coincidence with a particle in the DSSSD, with Doppler correction for ^{140}Sm. The $2_1^+ \rightarrow 0_1^+$ transition at 531 keV, the $4_1^+ \rightarrow 2_1^+$ transition at 715 keV, and the $2_2^+ \rightarrow 2_1^+$ transition at 460 keV are visible. The broad structure originates from the 871 keV $2_1^+ \rightarrow 0_1^+$ transition in ^{94}Mo. The purple arrow marks the $2_1^+ \rightarrow 0_1^+$ transition of the potential beam contaminant ^{140}Nd.

FIG. 5. Background subtracted γ-ray spectrum in coincidence with a particle in the DSSSD, with Doppler correction for the ^{94}Mo recoils. The $2_1^+ \rightarrow 0_1^+$ transition in ^{94}Mo was observed at 871 keV. The inset shows an enlarged part of the same spectrum, where the $3/2^+ \rightarrow 5/2_{\mathrm{gs}}^+$ transition in the target contaminant ^{95}Mo is seen at 204 keV.

of insufficient separation between the projectiles and target nuclei. The inverse kinematics with heavier projectiles and lighter target nuclei leads to an ambiguity where different center-of-mass scattering angles result in the same laboratory detection angle for the ^{140}Sm projectiles, which is further complicated by the low-energy cutoff for projectiles with the largest center-of-mass scattering angles. For this reason, the detection angle of the recoiling target nuclei was used to determine the center-of-mass scattering angle. For those center-of-mass scattering angles where both projectiles and recoiling target nuclei are expected to hit the sensitive region of the DSSSD, it was required that both particles were detected in opposite quadrants of the detector. The reaction kinematics and the hit pattern in the DSSSD were furthermore used to verify that the beam was well centered.

The γ rays detected in MINIBALL are Doppler shifted depending on the velocity and angle with respect to the emitting particle. Because it is not possible to determine if a given γ ray is emitted from a ^{140}Sm or ^{94}Mo nucleus, two spectra are produced with the assumption that all γ rays are emitted by either the projectiles or target nuclei and by applying the appropriate Doppler correction using the information from the DSSSD. This procedure results in two spectra where some transitions were properly Doppler corrected and appear as sharp peaks, whereas others are very broad because of a wrong Doppler correction. As long as the sharp and broad peaks are not overlapping it is possible to determine the intensities of the transitions from the respective spectra.

Background subtracted spectra with Doppler correction for ^{140}Sm and ^{94}Mo are shown in Figs. 4 and 5, respectively. The $2_1^+ \rightarrow 0_1^+$ transition at 531 keV, the $4_1^+ \rightarrow 2_1^+$ transition at 715 keV, and the $2_2^+ \rightarrow 2_1^+$ transition at 460 keV are visible in the spectrum that is Doppler corrected for the ^{140}Sm velocity. A hint of a transition is visible at 774 keV, marked by a purple arrow in Fig. 4. The energy corresponds to the
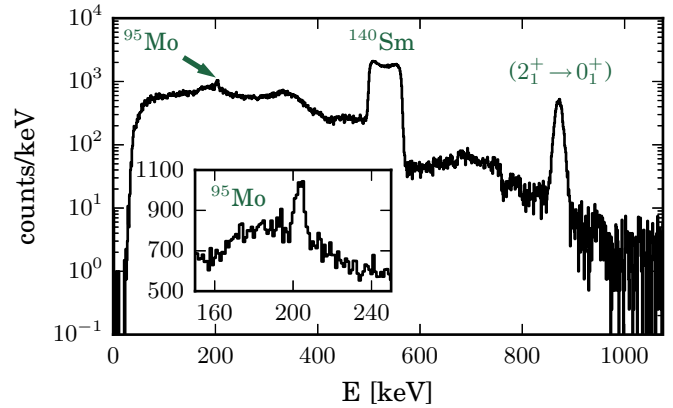
$2_1^+ \rightarrow 0_1^+$ transition in ^{140}Nd, which could be present as a contaminant in the beam. From the intensity of the transition this contamination is estimated to have an upper limit of 0.8% of the total beam intensity. The γ-ray energy spectrum with Doppler correction for the projectiles contains no indication of other beam contaminants.

The beam composition was monitored by performing regular measurements during which the RILIS lasers were periodically switched on and off. Figure 6 shows the spectra acquired during periods in which the lasers were turned on and off, respectively. Even in the spectrum with the lasers turned off only the $2_1^+ \rightarrow 0_1^+$ transition in ^{140}Sm is visible, although with much lower intensity compared to the spectrum taken with laser ionization. The acceleration of ^{140}Sm without laser is from surface ionization. The presence of any beam contaminants should be enhanced in the spectrum taken without lasers. The absence of any other transitions further supports the conclusion that the beam was composed of at
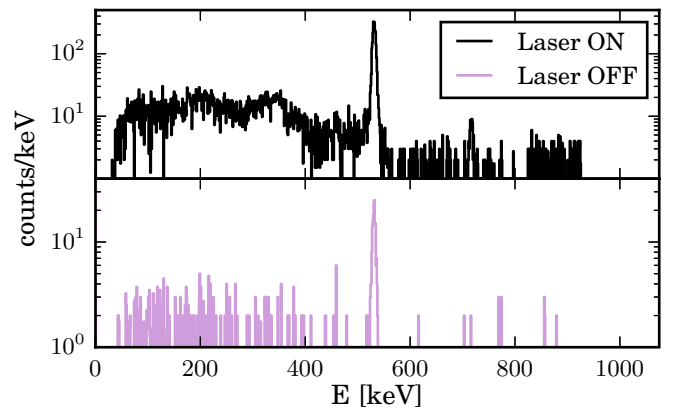

FIG. 6. Gamma-ray spectra obtained with and without RILIS laser ionization in a measurement during which the lasers were periodically switched on and off. The spectra are Doppler corrected for the ^{140}Sm projectiles.
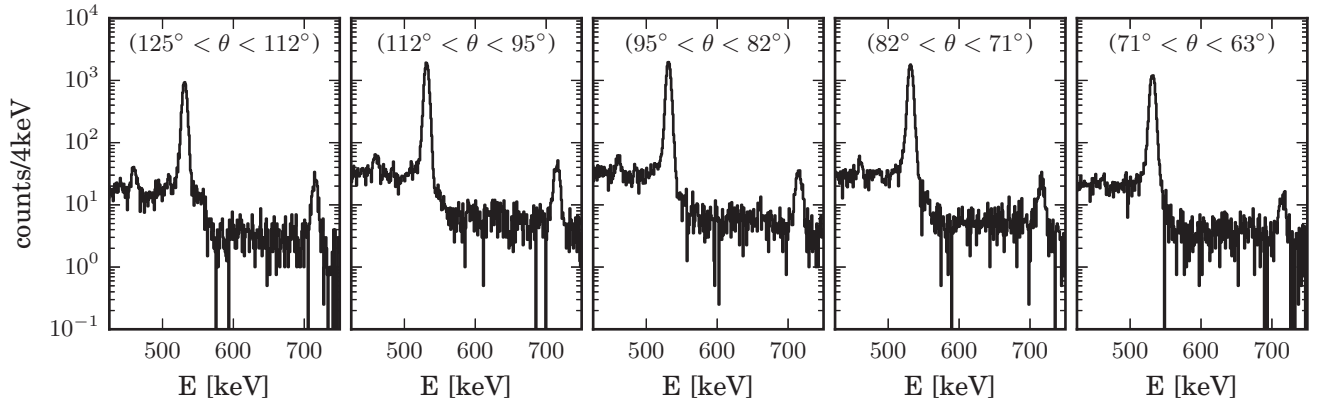
FIG. 7. Gamma-ray spectra for five separate ranges of center-of-mass scattering angles with Doppler correction for γ emission from the ^{140}Sm projectiles.

least 99.2% ^{140}Sm during the measurements with the lasers switched on.

An additional germanium detector was placed behind the beam dump downstream from MINIBALL to monitor the γ-ray spectra following the β decay of the beam particles. The spectra taken with this detector show no evidence for any radioactive beam contaminants. The small possible ^{140}Nd contaminant was considered negligible, and all further analysis was performed under the assumption that the ^{140}Sm beam was pure.

Figure 5 shows the total γ-ray spectrum with Doppler correction for the recoiling ^{94}Mo target nuclei. The $2_1^+ \rightarrow 0_1^+$ transition in ^{94}Mo at 871 keV is clearly visible, whereas the transitions in ^{140}Sm appear as broad structures. Closer inspection reveals a weak line at 204 keV. This peak is most likely from the $3/2^+ \rightarrow 5/2_{gs}^+$ transition in ^{95}Mo, which could be present as a small isotopic contamination in the target. This interpretation is supported by the fact that the same weak transition was also observed in previous experiments using the same target foil [29]. Because the electromagnetic matrix elements are well known for both ^{94}Mo [30] and ^{95}Mo [31], the amount of ^{95}Mo in the target can be determined from the Coulomb excitation analysis, as will be discussed below.

III. COULOMB EXCITATION DATA ANALYSIS

The analysis of the Coulomb excitation data and extraction of electromagnetic matrix elements utilizes the angular dependence of the differential Coulomb excitation cross sections. For this purpose, the data were subdivided into various ranges

of scattering angles as measured with the DSSSD. It was found that a division into five angular bins represents a good compromise between the maximum number of data points for differential cross sections and the minimum level of statistics in the spectra corresponding to each angular bin. The resulting spectra for five angular ranges and with Doppler correction for γ-ray emission from the ^{140}Sm projectiles are shown in Fig. 7. The spectra reveal how the relative strengths of the $4_1^+ \rightarrow 2_1^+$ and $2_2^+ \rightarrow 2_1^+$ transitions, which require two-step excitations, change with scattering angle compared to the $2_1^+ \rightarrow 0_1^+$ transition. The measured intensities for the three observed transitions in ^{140}Sm, the $2_1^+ \rightarrow 0_1^+$ transition in ^{94}Mo, and the $3/2_1^+ \rightarrow 5/2_{gs}^+$ transition in the target contaminant ^{95}Mo are listed in Table I for five angular ranges.

The coupled channel code GOSIA [32,33] was used to extract the electromagnetic matrix elements. The program combines semiclassical Coulomb excitation calculations with a multidimensional fitting procedure of the matrix elements. In this procedure, the set of matrix elements is found that best reproduces the measured γ-ray intensities observed for the different ranges of scattering angles, taking into account the geometry and efficiency of both particle and γ-ray detectors. Known lifetimes, branching ratios, and mixing ratios can be included in the χ^2 minimization. The γ-ray yields are obtained by integrating the Coulomb excitation cross section over the range of scattering angles covered by the experiment and integrating over the range of projectile energies resulting from the energy loss in the target. The measured γ-ray intensities were corrected for the relative efficiency values obtained from source calibrations. Finally, the correlated uncertainties were

TABLE I. Measured γ-ray intensities for all observed transitions for the five ranges of center-of-mass scattering angles. Values are rounded to two significant figures in the uncertainty.

	Transition	[63°, 71°]	[71°, 82°]	[82°, 95°]	[95°, 112°]	[112°, 125°]
^{140}Sm	$2_1^+ \rightarrow 0_1^+$	10200 ± 140	13840 ± 170	14350 ± 170	13780 ± 170	6860 ± 120
^{140}Sm	$4_1^+ \rightarrow 2_1^+$	118 ± 18	209 ± 24	286 ± 31	389 ± 34	199 ± 23
^{140}Sm	$2_2^+ \rightarrow 2_1^+$	47 ± 22	150 ± 33	239 ± 58	306 ± 60	300 ± 110
^{94}Mo	$2_1^+ \rightarrow 0_1^+$	743 ± 39	1073 ± 47	1213 ± 50	1090 ± 47	543 ± 34
^{95}Mo	$3/2_1^+ \rightarrow 5/2_{gs}^+$	175 ± 40	197 ± 45	249 ± 43	224 ± 53	179 ± 62

calculated for the set of reduced transitional and diagonal matrix elements.

To convert the measured γ-ray intensities into absolute cross sections, it is possible to normalize to the elastic Rutherford cross section obtained from particle-singles events. However, this requires precise knowledge of the particle detector efficiency, dead time, and beam intensity. The latter is often difficult to obtain with good precision in experiments with weak radioactive ion beams. In cases where the lifetime of one or more excited states are known, the corresponding reduced matrix element can be used to obtain absolute cross sections in the normalization procedure. Without prior knowledge of matrix elements, a different normalization technique is required. The GOSIA2 code [33,34] was developed to allow for the simultaneous analysis of both projectile and target excitation, using known reduced matrix elements for the scattering partners in the normalization. The ratio of observed transitions from the projectiles N_p and the target N_t is independent of the particle detection efficiency ϵ_{part} and the time-integrated luminosity L, as seen in Eq. (2):

$$\frac{N_p}{N_t} = \frac{L\epsilon_{\text{part}}b_p\epsilon_\gamma(E_p)\sigma_p}{L\epsilon_{\text{part}}b_t\epsilon_\gamma(E_t)\sigma_t}, \qquad (2)$$

where b_p and b_t are the γ-ray branching ratios, $\epsilon_\gamma(E_p)$ and $\epsilon_\gamma(E_t)$ the γ-ray efficiencies, and σ_p and σ_t the integrated cross sections for projectile and target excitation, respectively.

Two approaches were used in the data analysis from the current ^{140}Sm Coulomb excitation experiment. Because the low-spin structure of ^{140}Sm was initially unknown, the first approach was based on the normalization to the target excitation. After the measurement of the lifetime of the 2_1^+ state in ^{140}Sm [15] it was also possible to use the resulting $B(E2)$ value for normalization. A detailed description of both analysis approaches is presented below.

A. Normalization to the target excitation

Several criteria had to be considered for the choice of the target material in the Coulomb excitation experiment. Because the energy of the REX post-accelerator is limited to 3 A MeV, high-Z materials are disadvantageous because they would lead to large distances between the scattering partners and consequently to low cross sections. The mass of the target nucleus also has to be sufficiently different from the mass of the projectile to avoid ambiguities in the kinematics and ensure sufficient separation between the projectile and target nuclei in the plot of the particle energy as a function of scattering angle (c.f. Fig. 3). The energies of the γ-ray transitions in the projectile and target nuclei should be well separated to avoid overlapping peaks in the spectra. Finally, the matrix elements for the low-lying states should be well known to use the excitation of the target nucleus as normalization. It was found that ^{94}Mo was a suitable target material fulfilling the above criteria. The relevant electromagnetic matrix elements are known from Coulomb excitation experiments with α and ^{16}O projectiles [35,36].

As mentioned above, the observation of a transition at 204 keV in the spectrum that was Doppler corrected for the target recoils suggests the presence of ^{95}Mo in the target foil. The number of ^{95}Mo atoms N_{95}, relative to the number of ^{94}Mo atoms N_{94}, in the target foil can be found as

$$\frac{N_{95}}{N_{94}} = \frac{Y_{95}}{Y_{94}}\frac{\epsilon_{95}}{\epsilon_{94}}\frac{\sigma_{94}}{\sigma_{95}}, \qquad (3)$$

where Y_A and ϵ_A are the respective γ-ray yields and efficiencies for the $2_1^+ \rightarrow 0_1^+$ and $3/2^+ \rightarrow 5/2^+$ transitions in the two isotopes, and the cross sections σ_A for the populations of the 2_1^+ and $3/2^+$ states that are calculated from the known reduced matrix elements. An admixture of 4.4(11)% ^{95}Mo is found in this way, which is in good agreement with the value of 5(2)% that was found in another Coulomb excitation experiment using the same target foil [29].

An iterative procedure with alternating use of the codes GOSIA and GOSIA2 was employed to determine reduced matrix elements in ^{140}Sm with normalization to the target excitation. The procedure, which is explained in more detail elsewhere [34], is illustrated in Fig. 8 and summarized below.
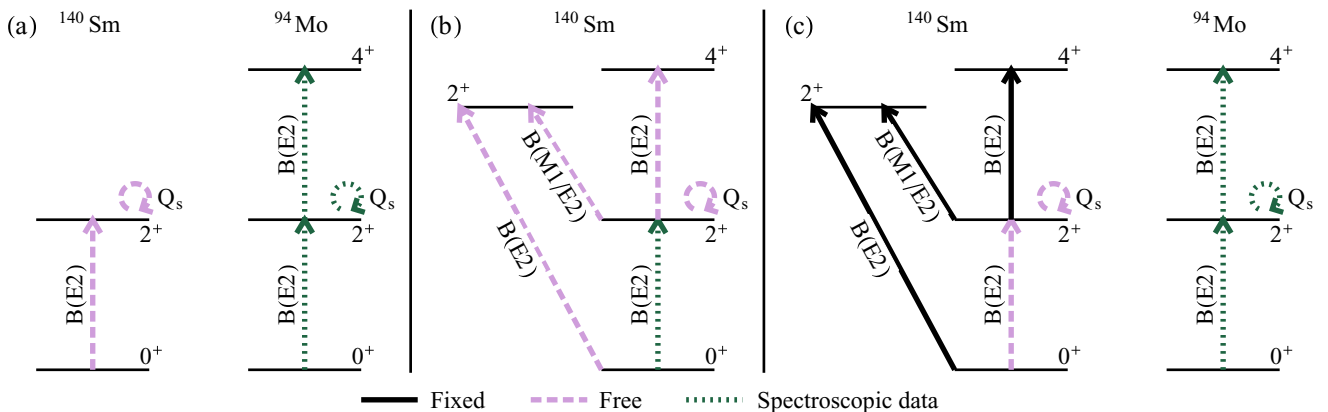
FIG. 8. Illustration of the iterative procedure to fit the reduced matrix elements using the codes GOSIA and GOSIA2, with parts (a), (b), and (c) corresponding to steps 2, 3, and 4 as described in the text. The level schemes indicate which matrix elements were included in the fit as free parameters, as fixed values, or as free parameters with spectroscopic data to constrain the fit. Iterations between step 3 and step 4 were performed until the solution converged.

TABLE II. Counts observed for the $2_1^+ \to 0_1^+$ transitions in the ^{140}Sm projectiles and the ^{94}Mo target nuclei and their uncertainties for 10 different ranges of scattering angles in the center-of-mass frame. These are the values used in the second step of the GOSIA-GOSIA2 iteration where $\theta_{\text{c.m.}} < 100°$. Values are rounded to two significant figures in the uncertainty.

Angular range	^{140}Sm	^{94}Mo
[95°, 100°]	4770 ± 240	397 ± 29
[90°, 95°]	3290 ± 160	245 ± 23
[86°, 90°]	4300 ± 220	351 ± 27
[82°, 86°]	5040 ± 250	450 ± 31
[78°, 82°]	5030 ± 250	439 ± 30
[75°, 78°]	4320 ± 230	311 ± 26
[71°, 75°]	4010 ± 200	323 ± 26
[68°, 71°]	4070 ± 200	310 ± 26
[66°, 68°]	3560 ± 180	250 ± 23
[63°, 66°]	2610 ± 130	206 ± 24

(1) In the first step, the standard GOSIA code is used for ^{94}Mo with the intensities of the $2_1^+ \to 0_1^+$ transition as input data and the known reduced matrix elements included as spectroscopic data. In this way an initial set of normalization factors was obtained.

(2) In the second step, the code GOSIA2 was used to simultaneously fit the reduced matrix elements in both ^{140}Sm and ^{94}Mo. The purpose of this step was to obtain a first estimate of the $\langle 0_1^+ \| E2 \| 2_1^+ \rangle$ matrix element in ^{140}Sm. Therefore only the matrix elements $\langle 0_1^+ \| E2 \| 2_1^+ \rangle$ and $\langle 2_1^+ \| E2 \| 2_1^+ \rangle$ and the γ-ray intensities for the $2_1^+ \to 0_1^+$ transition were included for ^{140}Sm [c.f. Fig. 8(a)]. To minimize the influence of multistep Coulomb excitation, only data for $\theta_{\text{c.m.}} < 100°$ were included in this step. With the high level of statistics for the $2_1^+ \to 0_1^+$ transition, the data could be divided into 10 angular ranges for this step, resulting in a better sensitivity for the $\langle 2_1^+ \| E2 \| 2_1^+ \rangle$ matrix element. The measured intensities for this subdivision of the data are given in Table II. With the normalization from step 1 as starting values, the χ^2 minimization yielded a new set of normalization factors and the $\langle 0_1^+ \| E2 \| 2_1^+ \rangle$ and $\langle 2_1^+ \| E2 \| 2_1^+ \rangle$ matrix elements for ^{140}Sm. Their uncertainties were obtained from the contour for $\chi^2_{\text{min}} + 1$ in a two-dimensional χ^2 map.

(3) In the third step, the standard GOSIA code was used for ^{140}Sm. The $\langle 0_1^+ \| E2 \| 2_1^+ \rangle$ matrix element obtained in step 2 and its uncertainty were treated as known spectroscopic data, whereas all other relevant matrix elements, $\langle 2_1^+ \| E2 \| 2_1^+ \rangle$, $\langle 2_1^+ \| E2 \| 4_1^+ \rangle$, $\langle 2_1^+ \| E2 \| 2_2^+ \rangle$, $\langle 2_1^+ \| M1 \| 2_2^+ \rangle$, and $\langle 0_1^+ \| E2 \| 2_2^+ \rangle$, were treated as free parameters [c.f. Fig. 8(b)]. In this step the γ-ray intensities from the division into five bins covering the entire angular range (c.f. Table I) were used to ensure sufficient statistics for the $4_1^+ \to 2_1^+$ and $2_2^+ \to 2_1^+$ transitions. An upper limit was included for the unobserved $2_2^+ \to 0_1^+$ transition. This step yielded a first realistic estimate of all relevant reduced matrix elements in ^{140}Sm.
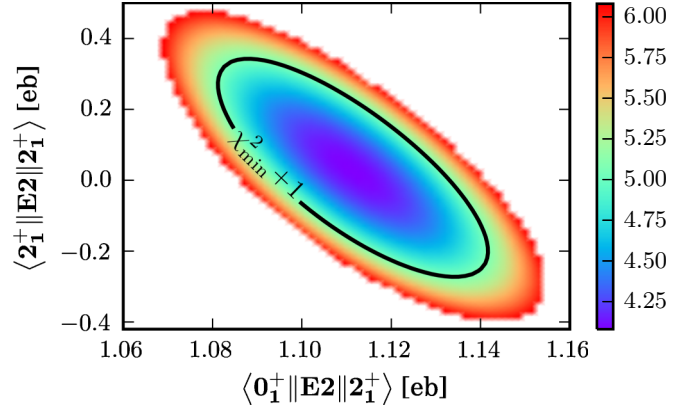

FIG. 9. Result of the χ^2 minimization for the $\langle 0_1^+ \| E2 \| 2_1^+ \rangle$ and $\langle 2_1^+ \| E2 \| 2_1^+ \rangle$ matrix elements in ^{140}Sm obtained after the last iteration of step 4 of the fitting procedure using target normalization. Note that the final uncertainties of all matrix elements were obtained after one more iteration of step 3.

(4) In the fourth step, the code GOSIA2 was again used for simultaneous χ^2 minimization of reduced matrix elements in ^{140}Sm and ^{94}Mo. Only the $\langle 0_1^+ \| E2 \| 2_1^+ \rangle$ and $\langle 2_1^+ \| E2 \| 2_1^+ \rangle$ matrix elements in ^{140}Sm were treated as free parameters; all other matrix elements for ^{140}Sm were fixed to the values from the previous step [c.f. Fig. 8(c)]. The γ-ray intensities from the division into five angular ranges were included for all observed transitions. This step yielded more realistic values for $\langle 0_1^+ \| E2 \| 2_1^+ \rangle$ and $\langle 2_1^+ \| E2 \| 2_1^+ \rangle$, because effects from coupling to higher-lying states were taken into account. Uncertainties for the free matrix elements were again taken from the $\chi^2_{\text{min}} + 1$ contour in the χ^2 map as shown in Fig. 9. In addition, a new set of normalization factors was obtained.

Steps three and four of the GOSIA-GOSIA2 iteration procedure were then repeated until the final solution stabilized. Overall uncertainties of all determined matrix elements were calculated by using the GOSIA code as the last stage of the data analysis. The resulting reduced matrix elements are presented in Table III. Reduced transition probabilities and spectroscopic quadrupole moments can be extracted from the transitional and diagonal matrix elements, respectively, using the following

TABLE III. Reduced matrix elements for ^{140}Sm and associated $B(E2)$ values and spectroscopic quadrupole moment with correlated errors obtained with the target normalization approach.

I_i	I_f	$\langle I_f \| E2 \| I_i \rangle$ [eb]	$B(E2; I_i \to I_f)$ [e^2b^2]
2_1^+	0_1^+	$1.11^{+0.03}_{-0.03}$	$0.25^{+0.02}_{-0.01}$
4_1^+	2_1^+	$1.63^{+0.05}_{-0.05}$	$0.30^{+0.02}_{-0.02}$
2_2^+	2_1^+	$1.33^{+0.08}_{-0.09}$	$0.35^{+0.05}_{-0.05}$
	I	$\langle I \| E2 \| I \rangle$ [eb]	$Q_s(I)$ [eb]
	2_1^+	$+0.03^{+0.54}_{-0.20}$	$+0.02^{+0.41}_{-0.15}$

TABLE IV. Reduced matrix elements for ^{140}Sm and associated $B(E2)$ values and spectroscopic quadrupole moment with correlated errors obtained with the lifetime normalization approach.

I_i	I_f	$\langle I_f \| E2 \| I_i \rangle$ [eb]	$B(E2; I_i \rightarrow I_f)$ [e^2b^2]
2_1^+	0_1^+	$1.02^{+0.04}_{-0.03}$	$0.21^{+0.02}_{-0.01}$
4_1^+	2_1^+	$1.61^{+0.05}_{-0.05}$	$0.29^{+0.02}_{-0.02}$
2_2^+	2_1^+	$1.32^{+0.08}_{-0.09}$	$0.35^{+0.04}_{-0.05}$
	I	$\langle I \| E2 \| I \rangle$ [eb]	$Q_s(I)$ [eb]
	2_1^+	$-0.17^{+0.51}_{-0.19}$	$-0.13^{+0.38}_{-0.14}$

relations:

$$B(E2; I_i \rightarrow I_f) = \frac{|\langle I_f \| E2 \| I_i \rangle|^2}{2I_i + 1}, \qquad (4)$$

$$Q_s(I) = \sqrt{\frac{16\pi}{5}} \frac{\langle II20|II\rangle}{\sqrt{2I+1}} \langle I \| E2 \| I \rangle, \qquad (5)$$

where $\langle II20|II\rangle$ is a Clebsch-Gordan coefficient. The data, and by consequence also the χ^2 minimization, was very insensitive to the $\langle 2_2^+ \| M1 | 2_1^+ \rangle$ matrix element, and no reliable value could be extracted. The $\langle 2_2^+ \| E2 \| 0_1^+ \rangle$ matrix element was also included in the analysis together with an upper limit for the intensity of the transition, which yielded an upper limit for the transition strength, $B(E2; 2_2^+ \rightarrow 0_1^+) < 0.001$ e^2b^2.

B. Normalization to the lifetime of the 2_1^+ state

The lifetime of the 2_1^+ state in ^{140}Sm was recently measured to be 9.1(6) ps in an experiment using the recoil-distance Doppler shift technique [15]. The resulting matrix element, $\langle 0_1^+ \| E2 \| 2_1^+ \rangle = 1.03(3)$ eb, can be used to normalize the Coulomb excitation data instead of normalizing to the excitation of the ^{94}Mo target nuclei. In this case, the lifetime is included as an additional data point in the χ^2 minimization within the standard GOSIA code. The χ^2 minimization is equivalent to step 3 in the iterative procedure described in Sec. III A and illustrated in Fig. 8. The reduced matrix elements obtained in this way are presented in Table IV. Note that the obtained matrix element $\langle 0_1^+ \| E2 \| 2_1^+ \rangle$ differ slightly from the value corresponding to the lifetime used as normalization. This is possible because the matrix element is allowed to vary in the χ^2 minimization to best fit all available data.

The resulting $B(E2; 2_1^+ \rightarrow 0_1^+)$ value reproduces the value from the lifetime measurement and is slightly smaller than the value obtained using the target normalization approach. It is interesting to note that the matrix elements connecting the 2_1^+ state with the 2_2^+ and 4_1^+ states are hardly affected and the values obtained with the lifetime normalization are almost identical to the ones obtained with target normalization. The quadrupole moment for the 2_1^+ state becomes slightly more negative when normalizing to the lifetime. However, the value is still rather small and the two results agree well within their uncertainty.

The small discrepancy between the two normalization approaches for the $\langle 2_1^+ \| E2 \| 0_1^+ \rangle$ matrix element could be from unaccounted-for systematic errors. One possible source

for such errors could be unknown target impurities. The discrepancy could also be from systematic errors for the lifetime of the 2_1^+ state in ^{140}Sm or for the matrix elements in the ^{94}Mo target nucleus.

C. State at 990 keV

In an earlier β-decay experiment the state at 990-keV excitation energy was tentatively assigned to have spin parity $I^\pi = (0^+)$ [13], but a more recent experiment revised this result and firmly assigned spin parity $I^\pi = 2^+$ to this state [14]. In the early stages of the analysis of the present Coulomb excitation experiment, the spin assignment for the state at 990 keV was not yet resolved, and the complete analysis, using both target and lifetime normalization approaches as described above, was performed with the assumption that the state at 990 keV had spin parity 0^+. The results concerning the 2_1^+ and 4_1^+ states were almost identical to the ones presented in Tables III and IV. However, the $\langle 0_2^+ \| E2 \| 2_1^+ \rangle$ matrix element yielded $B(E2; 0_2^+ \rightarrow 2_1^+) = 1.02(15)$ e^2b^2, which corresponds to 236 Weisskopf units. This very large transition probability was difficult to understand, and motivated the new experiment to measure the spin of the state at 990 keV using $\gamma - \gamma$ angular correlations. This experiment also found that the $2_2^+ \rightarrow 2_1^+$ transition is of almost pure $E2$ character with only a very small $M1$ admixture [14].

IV. DISCUSSION

The values using the target normalization approach are in good agreement with those obtained by normalizing to the measured lifetime of the 2_1^+ state. Only for the $\langle 2_1^+ \| E2 \| 0_1^+ \rangle$ reduced matrix element is a discrepancy of 1.8σ found between the two techniques. Both the target and lifetime normalization techniques rely on data from independent measurements. The former approach relies on reduced matrix elements for the ^{94}Mo target nucleus measured in separate Coulomb excitation experiments [35,36], whereas the latter relies on the lifetime of the 2_1^+ state in the ^{140}Sm projectiles from a recoil-distance Doppler shift measurement [15]. Without any obvious weaknesses in either approach or independent measurement, it is difficult to choose which results should be trusted more. We therefore adopt the average values from the two normalization methods for the following discussion. The adopted $B(E2)$ values are shown in Table V together with results from various theoretical calculations. The experimental excitation energies of the states are compared to the theoretical calculations in Fig. 10.

A. Geometric models

The spectroscopic quadrupole moment for the 2_1^+ state is consistent with zero, although the uncertainty is large. The spherical shape is inconsistent with an interpretation of the ground-state band as a rotational excitation with axial symmetry. An average spherical shape could indicate a quadrupole vibrational nature of the 2_1^+ state. However, the $B(E2; 4_1^+ \rightarrow 2_1^+)$ value is only insignificantly larger than the $B(E2; 2_1^+ \rightarrow 0_1^+)$ value, and not twice as large as would be required for a harmonic vibration. The energy

TABLE V. Comparison of experimental and theoretical B($E2$; $I_i \to I_f$) [e^2b^2] values and spectroscopic quadrupole moments, Q_s[eb] for ^{140}Sm.

I_i	I_f	Expt.	D1S	SM	IBA
2_1^+	0_1^+	0.23(2)	0.208	0.218	0.219
4_1^+	2_1^+	0.30(2)	0.338	0.314	0.326
6_1^+	4_1^+		0.455		0.379
2_2^+	2_1^+	0.35(5)	0.330	0.310	0.334
2_2^+	0_1^+	<0.001	2×10^{-5}	1.9×10^{-4}	2×10^{-4}
3_1^+	2_1^+		2×10^{-5}	2.3×10^{-4}	1×10^{-4}
3_1^+	2_2^+		0.396	0.362	0.277
0_2^+	2_1^+		0.138	0.008	0.126
0_2^+	2_2^+		2.6×10^{-3}	0.241	0.114
		Q_s[eb]			
2_1^+	2_1^+	$-0.06^{+0.41}_{-0.15}$	-0.12	-0.106	-0.140
2_2^+	2_2^+		0.11	0.113	0.043

ratio $E(4_1^+)/E(2_1^+) = 2.35$ is typical for a transitional nucleus between spherical and deformed shape. The fact that ^{140}Sm has a very low-lying 2_2^+ state supports the notion of triaxiality. Indeed, earlier investigations of the level structure of ^{140}Sm

have found that triaxial rotor calculations with moment of inertia parameters obtained from Woods-Saxon calculations could reproduce the excitation spectrum reasonably well [12]. As a first approach, it seems therefore natural to interpret the electromagnetic matrix elements within the simple triaxial rotor model, although its applicability for a weakly deformed even-even nucleus is not evident.

In the geometric model of Davydov and Filippov [37], the excitation energy of the 2_2^+ state is very sensitive to the degree of γ deformation. The lowest energy is found for maximum triaxiality of $\gamma = 30°$, where the 2_2^+ state is at twice the energy of the 2_1^+ state. Experimentally, the energy of the 2_2^+ state in ^{140}Sm is found to be even lower with $E(2_2^+)/E(2_1^+) = 1.86$ [14], which suggests that $\gamma = 30°$ should be used for the triaxial rotor model. For maximum triaxiality, the spectroscopic quadrupole moment $Q_s(2_1^+)$ should be zero, consistent with the present experimental result. Furthermore, the relative $E2$ strength of the $2_2^+ \to 2_1^+$ transition is expected to be $B(E2; 2_2^+ \to 2_1^+)/B(E2; 2_1^+ \to 0_1^+) = 10/7 = 1.43$, in good agreement with the experimental value of 1.52(25). This transition should only have a very small $M1$ component, which is again consistent with the present result and the $M1/E2$ mixing ratio extracted from the angular correlation measurement [14]. The $2_2^+ \to 0_1^+$ transition is strictly forbidden in the triaxial rotor model for
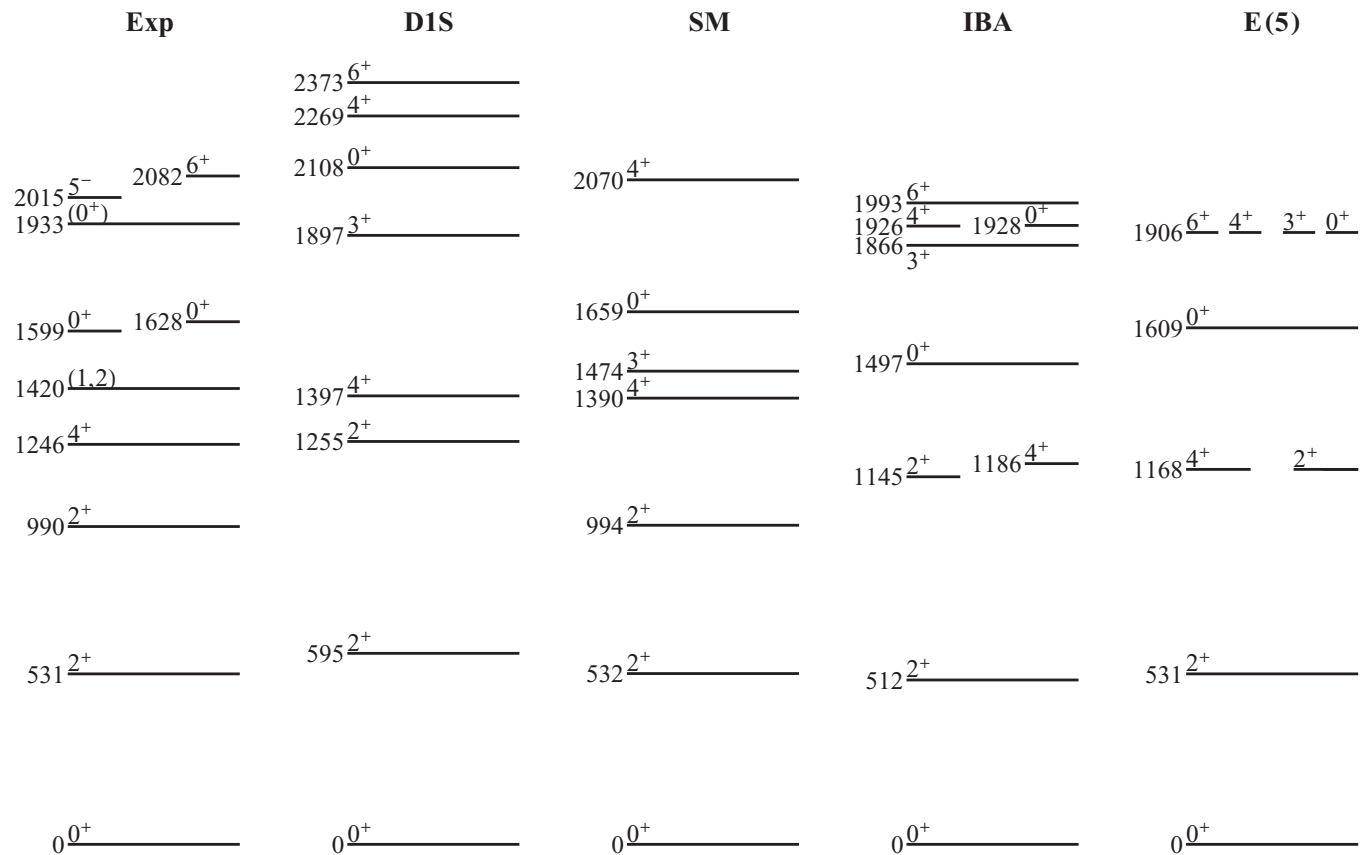

FIG. 10. Comparison of the experimental excitation energies (in keV) of the low-lying states in ^{140}Sm with predictions from beyond-mean-field calculations based on the Gogny D1S interaction, the shell model (SM), the interacting boson approximation (IBA), and expectations for a nucleus with E(5) critical point symmetry (see text for explanations).

$\gamma = 30°$. The experimental upper limit, $B(E2; 2_2^+ \to 0_1^+) <$ 0.001 e^2b^2, is indeed very low. The experimental energy ratio $E(4_1^+)/E(2_1^+) = 2.35$ is somewhat smaller than the value of 2.67 predicted by the Davydov-Filippov model, whereas the ratio $B(E2; 4_1^+ \to 2_1^+)/B(E2; 2_1^+ \to 0_1^+) = 1.30(14)$ agrees within errors with the expected value of 1.43.

The good agreement between the experimental relative transition strengths and the predictions of the triaxial rotor model for $\gamma = 30°$, in particular for the 2_2^+ state, suggests that the triaxial degree of freedom is important to understand the structure of the low-lying states in ^{140}Sm. It should be noted, however, that the relative $B(E2)$ strengths for surface vibrations in nuclei with γ-independent potential [38] are the same as for a triaxial rigid rotor. Indeed, it was found earlier that models based on the Wilets-Jean Hamiltonian are able to describe transitional nuclei in this mass region reasonably well [39]. Experimentally it is difficult to distinguish between γ-soft vibrational and γ-rigid rotational excitations. Coulomb excitation experiments are in principle able to distinguish between the two modes of excitation by providing complete sets of $E2$ matrix elements, which can be used to evaluate $E2$ invariants by summing over rotationally invariant zero-coupled products of $E2$ matrix elements [26]. Higher-order products are not only sensitive to the centroid, but also to the fluctuation widths of the $E2$ invariants. In practice, the technique is very challenging as incomplete knowledge of the matrix elements can strongly affect the results in particular for the higher-order products. The $E2$ matrix elements obtained in this work are insufficient to attempt an analysis of rotational invariants.

The best signature to distinguish between γ softness and γ rigidity is the energy staggering of the states in the $K = 2 \gamma$ band [40]. In the extreme γ-unstable limit, the states of the γ band form groups as (2_γ^+), $(3_\gamma^+, 4_\gamma^+)$, $(5_\gamma^+, 6_\gamma^+)$ [38], whereas for a rotor with maximum triaxiality the staggering leads to a grouping as $(2_\gamma^+, 3_\gamma^+)$, $(4_\gamma^+, 5_\gamma^+)$, etc. [37]. The states of the γ band beyond the 2_2^+ state are unfortunately not known for ^{140}Sm. The state at 1599-keV excitation energy that was tentatively assigned as the 3_γ^+ state in an earlier work [12] was shown to have spin parity $I^\pi = 0^{(+)}$ in the recent angular correlation measurement [14]. The identification of the 3_γ^+ and 4_γ^+ states would shed more light on the character of the axial asymmetry. Future Coulomb excitation experiments at higher beam energies and with heavier targets such as ^{208}Pb will populate these states with higher cross sections than the present experiment.

B. Algebraic models

Although the matrix elements related to the 2_2^+ state are well described by either γ-unstable or γ-rigid geometrical models, the discrepancies for the energies of the states indicate that these descriptions are too simple. The interacting boson approximation (IBA) was previously applied to describe transitional nuclei in this mass region [19]. The IBA parameters found to reproduce the experimental excitation energies of the lowest states place ^{140}Sm in between the spherical vibrational and the triaxially soft rotational limits of the IBA, which correspond to the SO(6) and U(5) subalgebras, respectively. The

transition between the SO(6) and U(5) dynamic symmetries was interpreted as a shape phase transition. At the critical point of this shape transition, the nuclear potential can roughly be approximated by a five-dimensional infinite well, in which case the Bohr Hamiltonian can be solved analytically and the wave functions be expressed in terms of Bessel functions [20]. Both ^{134}Ba and ^{128}Xe have been identified as good examples for this so-called E(5) critical point symmetry [41,42]. The predictions of the E(5) description for excitation energies and transition probabilities are parameter free except for overall scaling factors. To compare experimental data with the E(5) predictions, excitation energies and transition strengths are usually normalized to the energy of the 2_1^+ state and the $B(E2; 2_1^+ \to 0_1^+)$ value, respectively.

The nucleus ^{140}Sm was not considered as a candidate for E(5) critical point symmetry, mostly because of the previous assignment of the 990-keV level as a 0^+ state, which would be incompatible, and because experimental $B(E2)$ values were lacking. With the unambiguous identification of the states at 990 and 1599 keV as 2^+ and 0^+ states, respectively [14], and with the transition strengths obtained in this work, the hypothesis of ^{140}Sm as a candidate for E(5) critical point behavior can be evaluated. The excitation energies expected for a nucleus with E(5) symmetry are included in Fig. 10.

The excitation energies of the 4_1^+ and 2_2^+ states are expected to be equal with energy ratios $E(4_1^+)/E(2_1^+) = E(2_2^+)/E(2_1^+) = 2.20$ [20]. The experimental ratios of $E(4_1^+)/E(2_1^+) = 2.35$ and $E(2_2^+)/E(2_1^+) = 1.86$ are somewhat larger and smaller than the E(5) predictions, respectively. For the $B(E2)$ values, the E(5) model finds ratios of $B(E2; 4_1^+ \to 2_1^+)/B(E2; 2_1^+ \to 0_1^+) = B(E2; 2_2^+ \to 2_1^+)/B(E2; 2_1^+ \to 0_1^+) = 1.56$ when using the $E2$ operator of the IBA [43]. The experimental $B(E2)$ values obtained in the present work yield $B(E2; 4_1^+ \to 2_1^+)/B(E2; 2_1^+ \to 0_1^+) = 1.30(14)$ and $B(E2; 2_2^+ \to 2_1^+)/B(E2; 2_1^+ \to 0_1^+) = 1.52(25)$. It was argued that the excitation energies and decay patterns of excited 0^+ states provide a more stringent test of possible E(5) behavior than the properties of the 4_1^+ and 2_2^+ states [42]. In the E(5) description, the states $I_{\xi\tau}^\pi$ are characterized by the quantum numbers ξ and τ, which are related to the zeros of the Bessel functions [20]. The 0^+ state with $\xi = 2$ and $\tau = 0$, 0_{20}^+, should be the lowest in energy with $E(0_{20}^+)/E(2_1^+) = 3.03$ and it should decay predominantly to the 2_1^+ state with a branching ratio $B(E2; 0_{20}^+ \to 2_1^+)/B(E2; 0_{20}^+ \to 2_2^+) = 8.66$. The next 0^+ state has quantum numbers $\xi = 1$ and $\tau = 3$ with $E(0_{13}^+)/E(2_1^+) = 3.59$ and $B(E2; 0_{13}^+ \to 2_2^+)/B(E2; 0_{13}^+ \to 2_1^+) = 31.2$. Experimentally, the lowest excited 0^+ state is found at an excitation energy of 1599 keV with $E(0_2^+)/E(2_1^+) = 3.01$ and $B(E2; 0_2^+ \to 2_2^+)/B(E2; 0_2^+ \to 2_1^+) = 2.88$ [14]. Two more states with tentative 0^+ assignment were reported at excitation energies of 1629 keV $(E(0_3^+)/E(2_1^+) = 3.07)$ and 1933 keV $(E(0_4^+)/E(2_1^+) = 3.64)$. Both states were observed to decay only to the 2_1^+ state without decay branch to the 2_2^+ state [13]. Because only the 0_2^+ state at 1599 keV has a significant decay branch to the 2_2^+ state, it could be associated with the $\xi = 1$, $\tau = 3$ state of the E(5) model, although the branching ratio would be expected to be even more in favor of the 2_2^+ state. The 0_3^+ state at 1629 keV would then be a candidate for the

$\xi = 2$, $\tau = 0$ state based on its excitation energy and decay to the 2_1^+ state.

Although ^{140}Sm shows several features expected for a nucleus with E(5) symmetry, there are also deviations from the expected energy and $B(E2)$ ratios. The assumption of a nuclear potential that is independent of the deformation parameters β and γ is clearly too simple to describe the low-lying states in ^{140}Sm. The excitation spectrum of ^{140}Sm was reasonably well described in the past using the IBA, including the presence of a low-lying 2_2^+ state below the 4_1^+ state [12]. To investigate whether the IBA can also reproduce the measured transition strengths, calculations were performed using the proton-neutron version of the model, IBA-2, with the same set of parameters as in previous investigations (parameter set 2 from Ref. [12]). The resulting excitation spectrum is indeed very similar to the one corresponding to E(5) symmetry (c.f. Fig. 10), with the degeneracy of the multiplets only slightly lifted. However, this near degeneracy is not observed experimentally.

Effective charges of $e_\nu = 0.12$ and $e_\pi = 0.13$ for neutrons and protons, respectively, were found in a χ^2 minimization to reproduce the experimental $B(E2; 2_1^+ \rightarrow 0_1^+)$, $B(E2; 4_1^+ \rightarrow 2_1^+)$, and $B(E2; 2_2^+ \rightarrow 2_1^+)$ values. The values for the effective charges are similar to those found in previous investigations for this mass region [19]. The resulting $B(E2)$ values, which are included in Table V, are in good agreement with the experimental values. Furthermore, also the IBA-2 calculations find a vanishing $B(E2; 2_2^+ \rightarrow 0_1^+)$ value, and the calculated branching ratio $B(E2; 0_2^+ \rightarrow 2_2^+)/B(E2; 0_2^+ \rightarrow 2_1^+) = 0.90$ is of the same order of magnitude as the experimental value of 2.88 for the 0_2^+ state at 1599 keV. The calculated quadrupole moment for the 2_1^+ state is $Q_s(2_1^+) = -0.14\,eb$, consistent with the experimental value. It can be concluded that the interacting boson approximation is able to reproduce the excitation spectrum and transition strengths of ^{140}Sm reasonably well. However, the model relies on parameter fitting and effective charges to achieve this agreement, and its predictive power is therefore limited.

C. Shell model

Large-scale shell model calculations have been carried out including the $0g_{7/2}, 1d_{5/2}, 1d_{3/2}, 2s_{1/2}$, and $1h_{11/2}$ valence space for both protons and neutrons above a closed ^{100}Sn core. The effective GCN5082 [44] interaction is a realistic renormalized G matrix with phenomenological monopole constraints, which was used previously for the description of both low-lying and high-spin structures of nuclei with $50 \leqslant N, Z \leqslant 82$ [45–47]. The nucleus ^{140}Sm with 12 valence protons and 28 valence neutrons constitutes a numerical challenge for shell-model calculations at the limit of our present computing capability (m-scheme dimension $\sim 1.86 \times 10^{11}$), using the parallelized version of the Nathan shell-model code [48]. To reduce the basis dimension we introduce a truncation scheme with respect to the $1h_{11/2}$ orbital excitations, allowing all neutron excitations and up to four proton excitations to the $1h_{11/2}$ orbital.

The energies of the low-lying states obtained in the shell-model calculations are shown and compared to experimental
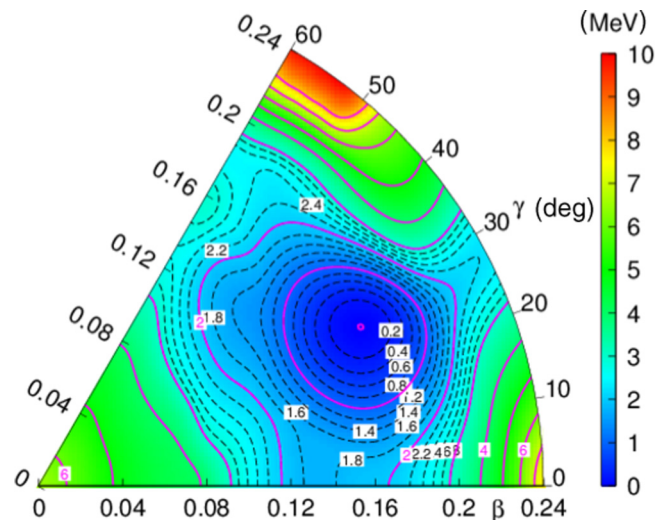

FIG. 11. Potential energy surface for ^{140}Sm from constrained deformed Hartee-Fock minimization in the shell-model basis.

data in Fig. 10. In general, a rather good agreement is found for both yrast and yrare states. The calculations reproduce the correct ordering of the states and in particular a low-lying 2_2^+ state. Transition rates were calculated using effective charges of $0.65e$ and $1.65e$ for neutrons and protons, respectively. The results are included in Table V and the $B(E2)$ values show a good agreement with the experimental data. Several features found for the 2_2^+ and 3_1^+ states support their interpretation as members of a $K = 2$ γ vibrational band: The quadrupole moments for the 2_1^+ and 2_2^+ states are almost equal but of opposite sign, the quadrupole moment for the 3_1^+ state is approximately zero, and it decays to the 2_2^+ state via a strong $E2$ transition.

Constrained Hartee-Fock calculations performed with the same shell-model Hamiltonian within the same valence space reveal the presence of a triaxial minimum at $\beta \sim 0.16$ and $\gamma = 26.5°$ as shown in Fig. 11. The potential energy surface is consistent with both the geometrical interpretation of the data and the electromagnetic matrix elements obtained in the shell-model calculations. The shell-model calculations support the notion of triaxial deformation as the most salient feature of the ^{140}Sm nucleus, with a well-developed γ-soft band built on the 2_2^+ state that is dominated by $2p2h$ proton excitations.

D. Beyond-mean-field model

We have calculated the energies of the low-lying states and the transition strengths between them using microscopic calculations based on constrained Hartree-Fock-Bogoliubov (CHFB) theory using the Gogny D1S interaction [49,50] and mapping to the five-dimensional collective Hamiltonian (5DCH) for quadrupole excitations at low energy. The method was described in detail elsewhere [2], and results for the $B(E2; 2_1^+ \rightarrow 0_1^+)$ values for the chain of neutron-deficient even-even samarium isotopes were presented in the context of the recent lifetime measurement in ^{140}Sm [15], where it was demonstrated that the calculations are able to correctly describe the onset of quadrupole collectivity for the samarium isotopes below the $N = 82$ shell closure. It should be
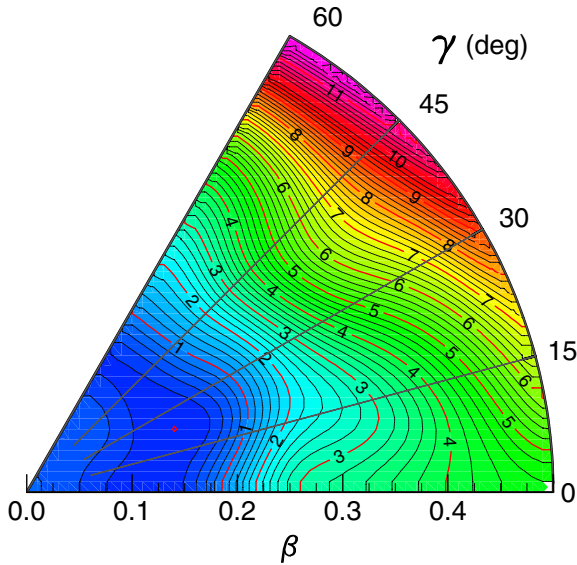
FIG. 12. Potential energy surface for the ground state of ^{140}Sm obtained in the CHFB calculations with the Gogny D1S interaction.

noted that the CHFB+5DCH calculations contain no free parameters except for those specifying the phenomenological D1S interaction, which is globally used across the entire nuclear chart. Figure 12 shows the potential energy surface obtained from the CHFB calculations. A shallow minimum is found for quadrupole deformation parameters $\langle \beta \rangle = 0.17$ and $\langle \gamma \rangle = 29°$, indicated by a red dot in Fig. 12. The location of the potential energy minimum is consistent with the result from the shell model (c.f. Fig. 11). However, compared to the latter, the potential energy surface found in the CHFB calculations reveals considerably more γ softness. The fluctuation parameters [51] of $\Delta \beta = 0.046$ and $\Delta \gamma = 13°$ indicate a significant spreading of the ground-state wave function in particular in the γ direction.

The excitation spectrum for ^{140}Sm obtained in the CHFB+5DCH calculations for all positive-parity states up to the 6_1^+ state is included in Fig. 10. The general features of the excitation spectrum are well reproduced. The energies of the states in the ground-state band are overestimated by 10%–15%. It was noted previously that the excitation energy of excited 0^+ states are systematically overpredicted [2]. This is also the case for ^{140}Sm, where the discrepancy is approximately 30%. The 2_2^+ state is found to have predominant $K = 2$ character, consistent with a γ-vibrational excitation. The calculations reproduce the relative position of the 2_2^+ state slightly below the 4_1^+ state. The 3_1^+ and 4_2^+ states can be interpreted as members of the $K = 2$ γ band. The energy spacing of the states in the γ band is consistent with a γ-soft potential as evidenced by the potential energy surface.

The calculated $B(E2)$ values are presented in Table V. The comparison with the experimental values shows very good agreement. The calculations find almost identical $B(E2)$ values for the $4_1^+ \rightarrow 2_1^+$ and $2_2^+ \rightarrow 2_1^+$ transitions and an almost vanishing $B(E2)$ value for the $2_2^+ \rightarrow 0_1^+$ transition, consistent both with the experimental results and the geometric interpretation of maximum triaxiality. The calculated quadrupole

moment for the 2_1^+ state is $Q_s(2_1^+) = -0.12\ eb$, corresponding to a very small prolate deformation, in good agreement with the experimental value. The calculated quadrupole moment for the 2_2^+ state, $Q_s(2_2^+) = +0.12\ eb$, has the same magnitude and opposite sign compared to the quadrupole moment of the 2_1^+ state, $Q_s(2_1^+)$, giving further support for the interpretation of the 2_2^+ state as the head of a γ-vibrational band. As expected for such a band, the 3_1^+ state decays predominantly to the 2_2^+ state and has an almost vanishing quadrupole moment, $Q_s(3_1^+) = -0.01\ eb$. As a whole, the calculations support the simple geometric picture of ^{140}Sm as a nucleus with pronounced triaxiality and γ softness and provide a fully microscopic foundation for this interpretation.

V. SUMMARY

A low-energy Coulomb excitation experiment to study electromagnetic transition probabilities and spectroscopic quadrupole moments in ^{140}Sm was performed at the REX-ISOLDE facility at CERN. A quasipure beam of ^{140}Sm was produced by proton-induced spallation of a primary tantalum target followed by resonant laser ionization. The radioactive ions were accelerated to an energy of $2.85A$ MeV and scattered on a secondary ^{94}Mo target. Scattered projectiles and recoiling target nuclei were detected in a highly segmented silicon detector at forward angles, while γ rays were measured with the MINIBALL array of segmented HPGe detectors. The code GOSIA was used to extract transitional and diagonal electromagnetic matrix elements from the γ-ray yields observed as a function of scattering angle. By normalizing the yields to known reduced matrix elements for the ^{94}Mo target and the known lifetime of the 2_1^+ state, it was possible to determine several $B(E2)$ values for transitions between low-lying states and the spectroscopic quadrupole moment of the 2_1^+ state in ^{140}Sm.

The experimental electromagnetic matrix elements were compared to the results of large-scale shell-model calculations and to calculations based on constrained Hartree-Fock-Bogoliubov theory using the Gogny D1S interaction and mapping to a five-dimensional collective Hamiltonian. A clear picture emerges from the comparison between experimental and theoretical results that relate the observed structures in ^{140}Sm to a weak quadrupole deformation with maximum triaxiality of $\gamma \approx 30°$ and significant γ softness. The analysis of the excitation spectrum and the transition probabilities using the interacting boson model suggests that ^{140}Sm exhibits many of the features expected for a nucleus with approximate E(5) critical point symmetry.

To learn more about the degree of γ softness it would be desirable to identify the states of the γ-vibrational band beyond the 2_2^+ state and to measure transition probabilities connected to the states in the γ-vibrational band and to the excited 0^+ states. With the higher beam energies provided by the new HIE-ISOLDE post-accelerator and the resulting higher cross sections, such measurements will become feasible in the future.

[1] A. Bohr and B. R. Mottelson, *Nuclear Structure*, Vol. II (W. A. Benjamin, Reading, 1975).

[2] J.-P. Delaroche, M. Girod, J. Libert, H. Goutte, S. Hilaire, S. Péru, N. Pillet, and G. F. Bertsch, Phys. Rev. C **81**, 014303 (2010).

[3] J. Dobaczewski, M. V. Stoitsov, and W. Nazarewicz, AIP Conf. Proc. **726**, 51 (2004).

[4] K. Heyde and J. L. Wood, Rev. Mod. Phys. **83**, 1467 (2011).

[5] J. L. Wood and K. Heyde, J. Phys. G **43**, 020402 (2016).

[6] A. N. Andreyev, M. Huyse, P. Van Duppen, L. Weissman, D. Ackermann, J. Gerl, F. P. Hessberger, S. Hofmann, A. Kleinbohl, G. Munzenberg, S. Reshitko, C. Schlegel, H. Schaffner, P. Cagarda, M. Matos *et al.*, Nature (London) **405**, 430 (2000).

[7] N. Bree, K. Wrzosek-Lipska, A. Petts, A. Andreyev, B. Bastin, M. Bender, A. Blazhev, B. Bruyneel, P. A. Butler, J. Butterworth, M. P. Carpenter, J. Cederkäll, E. Clément, T. E. Cocolios, A. Deacon *et al.*, Phys. Rev. Lett. **112**, 162701 (2014).

[8] W. Starzecki, G. D. Angelis, B. Rubio, J. Styczen, K. Zuber, H. Güven, W. Urban, W. Gast, P. Kleinheinz, S. Lunardi, F. Soramel, A. Facco, C. Signorini, M. Morando, W. Meczynski *et al.*, Phys. Lett. B **200**, 419 (1988).

[9] M. A. Cardona, S. Lunardi, D. Bazzacco, G. de Angelis, and V. Roca, Phys. Rev. C **44**, 891 (1991).

[10] G. Lalazissis, M. Sharma, and P. Ring, Nucl. Phys. A **597**, 35 (1996).

[11] T. Nikšić, P. Ring, D. Vretenar, Y. Tian, and Z.-y. Ma, Phys. Rev. C **81**, 054318 (2010).

[12] B. D. Kern, R. L. Mlekodaj, G. A. Leander, M. O. Kortelahti, E. F. Zganjar, R. A. Braga, R. W. Fink, C. P. Perez, W. Nazarewicz, and P. B. Semmes, Phys. Rev. C **36**, 1514 (1987).

[13] R. B. Firestone, J. Gilat, J. M. Nitschke, P. A. Wilmarth, and K. S. Vierinen, Phys. Rev. C **43**, 1066 (1991).

[14] J. Samorajczyk, M. Klintefjord, C. Droste, A. Görgen, T. Marchlewski, J. Srebrny, T. Abraham, F. L. B. Garrote, E. Grodner, K. Hadyńska-Klęk, M. Kisieliński, M. Komorowska, M. Kowalczyk, J. Kownacki, P. Napiorkowski, R. Szenborn, A. Stolarz, A. Tucholski, and G. M. Tveten, Phys. Rev. C **92**, 044322 (2015).

[15] F. L. Bello Garrote, A. Görgen, J. Mierzejewski, C. Mihai, J.-P. Delaroche, M. Girod, J. Libert, E. Sahin, J. Srebrny, T. Abraham, T. K. Eriksen, F. Giacoppo, T. W. Hagen, M. Kisielinski, M. Klintefjord *et al.*, Phys. Rev. C **92**, 024317 (2015).

[16] R. F. Casten, D. D. Warner, D. S. Brenner, and R. L. Gill, Phys. Rev. Lett. **47**, 1433 (1981).

[17] F. Iachello, Phys. Rev. Lett. **87**, 052502 (2001).

[18] R. F. Casten and N. V. Zamfir, Phys. Rev. Lett. **87**, 052503 (2001).

[19] S. Pascu, N. V. Zamfir, G. Căta-Danil, and N. Mărginean, Phys. Rev. C **81**, 054321 (2010).

[20] F. Iachello, Phys. Rev. Lett. **85**, 3580 (2000).

[21] V. N. Fedosseev, L.-E. Berg, D. V. Fedorov, D. Fink, O. J. Launila, R. Losito, B. A. Marsh, R. E. Rossel, S. Rothe, M. D. Seliverstov, A. M. Sjödin, and K. D. A. Wendt, Rev. Sci. Instrum. **83**, 02A903 (2012).

[22] F. Schwellnus, R. Catherall, B. Crepieux, V. Fedosseev, B. Marsh, C. Mattolat, M. Menna, F. Österdahl, S. Raeder, T. Stora, and K. Wendt, Nucl. Instrum. Methods B **267**, 1856 (2009).

[23] P. Schmidt, F. Ames, G. Bollen, O. Forstner, G. Huber, M. Oinonen, and J. Zimmer, Nucl. Phys. A **701**, 550 (2002).

[24] F. Wenander, Nucl. Phys. A **701**, 528 (2002).

[25] O. Kester, T. Sieber, S. Emhofer, F. Ames, K. Reisinger, P. Reiter, P. Thirolf, R. Lutter, D. Habs, B. Wolf, G. Huber, P. Schmidt, A. Ostrowski, R. von Hahn, R. Repnow *et al.*, Nucl. Instrum. Methods B **204**, 20 (2003).

[26] D. Cline, Annu. Rev. Nucl. Sci. **36**, 683 (1986).

[27] N. Warr, J. Van de Walle, M. Albers, F. Ames, B. Bastin, C. Bauer, V. Bildstein, A. Blazhev, S. Bönig, N. Bree, B. Bruyneel, P. Butler, J. Cederkäll, E. Clément, T. Cocolios *et al.*, Eur. Phys. J. A **49**, 40 (2013).

[28] A. Ostrowski, S. Cherubini, T. Davinson, D. Groombridge, A. Laird, A. Musumarra, A. Ninane, A. di Pietro, A. Shotter, and P. Woods, Nucl. Instrum. Methods A **480**, 448 (2002).

[29] N. Kesteloot, B. Bastin, L. P. Gaffney, K. Wrzosek-Lipska, K. Auranen, C. Bauer, M. Bender, V. Bildstein, A. Blazhev, Bönig *et al.*, Phys. Rev. C **92**, 054301 (2015).

[30] D. Abriola and A. Sonzogni, Nucl. Data Sheets **107**, 2423 (2006).

[31] S. Basu, G. Mukherjee, and A. Sonzogni, Nucl. Data Sheets **111**, 2555 (2010).

[32] T. Czosnyka, D. Cline, and C. Wu, Bull. Am. Phys. Soc. **28**, 745 (1983).

[33] "GOSIA manual", http://www.pas.rochester.edu/~cline/Gosia (2011).

[34] M. Zielińska, L. P. Gaffney, K. Wrzosek-Lipska, E. Clément, T. Grahn, N. Kesteloot, P. Napiorkowski, J. Pakarinen, P. Van Duppen, and N. Warr, Eur. Phys. J. A **52**, 99 (2016).

[35] J. Barrette, M. Barrette, A. Boutard, R. Haroutunian, G. Lamoureux, and S. Monaro, Phys. Rev. C **6**, 1339 (1972).

[36] P. Paradis, G. Lamoureux, R. Lecomte, and S. Monaro, Phys. Rev. C **14**, 835 (1976).

[37] A. Davydov and G. Filippov, Nucl. Phys. **8**, 237 (1958).

[38] L. Wilets and M. Jean, Phys. Rev. **102**, 788 (1956).

[39] S. G. Rohoziński, J. Srebrny, and K. Horbaczewska, Z. Phys. **268**, 401 (1974).

[40] N. Zamfir and R. Casten, Phys. Lett. B **260**, 265 (1991).

[41] R. F. Casten and N. V. Zamfir, Phys. Rev. Lett. **85**, 3584 (2000).

[42] R. M. Clark, M. Cromaz, M. A. Deleplanque, M. Descovich, R. M. Diamond, P. Fallon, I. Y. Lee, A. O. Macchiavelli, H. Mahmud, E. Rodriguez-Vieitez, F. S. Stephens, and D. Ward, Phys. Rev. C **69**, 064322 (2004).

[43] J. M. Arias, Phys. Rev. C **63**, 034308 (2001).

[44] A. Gniady, E. Caurier, and F. Nowacki (unpublished).

[45] K. Sieja, G. Martínez-Pinedo, L. Coquard, and N. Pietralla, Phys. Rev. C **80**, 054311 (2009).

[46] E. Caurier, F. Nowacki, A. Poves, and K. Sieja, Phys. Rev. C **82**, 064304 (2010).

[47] C. M. Petrache, I. Ragnarsson, H. Naïdja, F. Nowacki, R. Leguillon, T. Zerrouki, P. T. Greenlees, U. Jakobsson, P. Jones, R. Julin, S. Juutinen, S. Ketelhut, M. Leino, M. Nyman, P. Peura, P. Rahkila, P. Ruotsalainen, J. Saren, C. Scholey, J. Sorri, and J. Uusitalo, Phys. Rev. C **92**, 034314 (2015).

[48] E. Caurier, G. Martínez-Pinedo, F. Nowacki, A. Poves, and A. P. Zuker, Rev. Mod. Phys. **77**, 427 (2005).

[49] J. Dechargé and D. Gogny, Phys. Rev. C **21**, 1568 (1980).

[50] J. Berger, M. Girod, and D. Gogny, Comput. Phys. Commun. **63**, 365 (1991).

[51] J. Libert, M. Girod, and J.-P. Delaroche, Phys. Rev. C **60**, 054301 (1999).